

Multiscale Dynamical Processes Underlying the Wintertime Atlantic Blockings

JIWANG MA

*School of Atmospheric Sciences, Nanjing University of Information Science and Technology, Nanjing,
and Shandong Meteorological Observatory, Jinan, China*

X. SAN LIANG

*School of Marine Sciences, and School of Atmospheric Sciences, Nanjing University of Information Science and Technology,
Nanjing, China*

(Manuscript received 19 October 2016, in final form 11 July 2017)

ABSTRACT

The wintertime atmospheric blocking over the Atlantic is investigated using a newly developed methodology—namely, localized multiscale energy and vorticity analysis (MS-EVA)—and the theory of canonical energy transfer. Through a multiscale window transform (MWT), the atmospheric fields from the ERA-40 data are reconstructed on three-scale ranges or scale windows: basic-flow window, blocking window, and synoptic window. The blocking event is obtained by compositing the wintertime blocking episodes, and a clear westward-retrograding signal is identified on the blocking window. Likewise, the local multiscale energetics following the signal are composited. It is found that a life cycle of the blocking-scale kinetic energy (KE) may be divided into three phases: onset phase, amplification phase, and decay phase. Different phases have different mechanisms in play. In general, pressure work and the canonical transfer from the synoptic eddies initiate the generation of the blocking, while the latter contributes to its amplification. The blocking decays as the system transports the KE away and as it converts the KE into available potential energy (APE) through buoyancy conversion. For the APE on the blocking window, its evolution experiences two maxima and, correspondingly, two phases can be distinguished. In the first maximum phase, the dominating mechanism is baroclinic instability; in the second, buoyancy conversion takes place. These are also the mechanisms that cause the warm core of the blocking in the troposphere.

1. Introduction

Atmospheric blocking is a nearly stationary process that lasts for more than a week during which the zonal jet stream is interrupted and split into two branches. Although difficult to define in an exact way (Lejenäs and Økland 1983), it is generally characterized by 1) a double-jet system extending over at least 45° of longitude and 2) a pattern persistent over one region for 5–30 days (e.g., Berggren et al. 1949; Rex 1950b; Austin 1980; Treidl et al. 1981; Charney et al. 1981; Tibaldi and Molteni 1990). It causes the affected regions to have the same weather for an extended period of time, typically with more precipitation in the south and less at higher latitudes (Trigo et al. 2004; Sousa et al. 2016). Its influence on the ambient weather and climate has been extensively investigated (e.g., Namias 1947; Berggren et al. 1949; Rex 1950a,b); this

has made it one of the most studied processes in the atmospheric sciences.

As we know, the typical lifetime of synoptic eddies is no more than one week, while a substantial proportion of blocking episodes last for much longer. Besides, synoptic eddies always propagate eastward in the westerlies, while blockings are almost stationary and even retrograde. What is more, blockings have relative large amplitudes. These imply that nonlinearity may be important. Nonlinear theoretical models have been proposed (Charney and DeVore 1979; McWilliams 1980; Shutts 1983; Yamazaki and Itoh 2013; Luo et al. 2014), among which are, particularly, the model of equivalent modons (McWilliams 1980), the soliton model (Huang et al. 2007; Lou and Huang 2017), and the multiscale interaction model (Luo et al. 2014). While indeed these theories have been successful in their respective contexts, what nature really chooses is not quite clear. For this reason, many other scientists choose to diagnose the processes for an

Corresponding author: X. San Liang, sanliang@courant.nyu.edu

DOI: 10.1175/JAS-D-16-0295.1

© 2017 American Meteorological Society. For information regarding reuse of this content and general copyright information, consult the [AMS Copyright Policy](http://www.ametsoc.org/PUBSReuseLicenses) (www.ametsoc.org/PUBSReuseLicenses).

understanding of them. This includes the diagnoses of momentum flux (Green 1977; Austin 1980), heat flux (Austin 1980; Illari and Marshall 1983), potential vorticity (Illari 1984), and geopotential height (Tsou and Smith 1990), to name a few. In this study, we focus on the diagnostics of multiscale energetics.

Ever since Lorenz (1955) introduced the concept of energy cycle, multiscale energetic diagnosis has become a powerful tool for atmospheric research. For the blocking study, this has been extensively used. For example, Holopainen and Fortelius (1987) discuss the energy transfer between the high-frequency (less than 6 days) eddies and the 10-day mean flow during blocking and identify an enhanced transfer of eddy kinetic energy (KE) to the mean flow over the storm tracks in the blocking case. Hansen and Chen (1982) investigate two blockings using spectral energetics analysis, one occurring over Atlantic and another over Pacific, and find that the nonlinear interaction between the cyclone-scale and planetary-scale waves is essential to the Atlantic blocking, while baroclinic amplification plays the most important role in the formation of the Pacific one. Hansen and Sutera (1984) demonstrate that the critical difference in energetics between blocking and non-blocking periods lies in the nonlinear interaction term. However, zonal spectral analyses are inconclusive because they cannot distinguish between processes near to or far from the block. For this reason, Fournier (2002, 2003) uses orthogonal wavelet analysis to investigate the local information of KE transfer between different scales during a blocking process and finds that the KE transfer is upscale from the eddies in the upstream of the blocking and downscale in the downstream.

Since the center of a blocking may be on the move and its strength changes with time, information local in both space and time is needed to explain its evolution. Among the methods as we mention above in previous studies, only the orthonormal wavelet analysis can give local information. However, given its multiresolution nature, in a discrete wavelet domain how the moving pattern in space–time can be handled is still unclear. Besides, a blocking generally involves many different scales. A single wavelet scale is not enough to describe it; to remedy, Fournier (2005) sums over some designated individual scales to construct a physically meaningful mode that bears resemblance to blocking. But even so, if the block moves significantly then this reconstruction is still unsatisfactory. The underlying problem is that “moving” as a concept in a continuous space–time implies spurious changes in a discrete orthonormal wavelet domain [cf. Fournier (2000), his Eq. (D4)].

We hence need a methodology that is capable of handling the blocking process, which is in nature

highly nonlinear, multiscale interactive, and localized in space and time. The localized multiscale energy and vorticity analysis (MS-EVA) recently developed by Liang and Robinson (2005, 2007) is just such a methodology. MS-EVA is based on a new functional analysis apparatus called multiscale window transform (MWT), which may be simply understood as an orthogonal decomposition according to scale ranges, while has the local information retained. Our purpose here is, using the MS-EVA and the MS-EVA-based theories, to investigate the dynamical processes underlying the evolution—including the onset, development, and decay—of the blockings. Some studies (Nakamura et al. 1997; Schneidereit et al. 2012; Park et al. 2015; Pelly and Hoskins 2003; Colucci 1985) show that both synoptic and low-frequency processes play important roles in the blocking evolution, so a three-scale separation will be performed. We will focus specifically on the blockings over the Atlantic Ocean, since the Atlantic is found to be one of the preferred blocking regions (Lejenäs and Økland 1983). In the following we will first give a brief introduction of MWT, MS-EVA, and the MS-EVA-based theory of barotropic and baroclinic instabilities. Section 3 is devoted to a description of the composited blocking and the reconstructed signals on the multiscale windows, and sections 4 and 5 provide an analysis of the resulting multiscale energetics. Some issues are discussed in section 6. The whole study is concluded in section 7.

2. Data and method

a. Data

The ERA-40 (<http://apps.ecmwf.int/datasets/data/era40-daily/levtype=pl/>) dataset (Uppala et al. 2005) will be used for our study. It includes temperature (T), wind components (u , v , ω), and geopotential (Φ) from the European Centre for Medium-Range Weather Forecasts (ECMWF). For our purpose, we choose a time resolution of 6 h and a spatial resolution of $2.5^\circ \times 2.5^\circ$. The spatial domain covers the zonal circle between 30° and 87.5°N and 15 standard p levels from 1000 to 50 hPa. As it is required in the analysis that the number of the time steps should be a power of 2, the data period is chosen to be 1 September 1957–21 May 2002, which results in series with 2^{16} time steps.

b. Blocking index

The blocking index proposed by Lejenäs and Økland (1983) and modified by Tibaldi and Molteni (1990) (called TM index herein) has been extensively used in

the blocking studies. We hence use this index though we notice that some new indices have been proposed. We use it to pick up blocking episodes during the whole range of the period based on a criterion, with two quantities:

$$\text{GHGS} = \frac{Z(\phi_0) - Z(\phi_s)}{(\phi_0 - \phi_s)} \quad \text{and}$$

$$\text{GHGN} = \frac{Z(\phi_n) - Z(\phi_0)}{(\phi_n - \phi_0)},$$

where GHGS and GHGN represent the southern and northern parts of the 500-hPa geopotential height (Z) gradient, respectively, and ϕ denotes latitude and $\phi_n = 80 + \Delta$, $\phi_0 = 60 + \Delta$, and $\phi_s = 40 + \Delta$, while Δ is a parameter with a value of -5 , 0 , or 5 , as suggested by the Climate Prediction Center (<http://www.cpc.ncep.noaa.gov/products/precip/CWlink/blocking/index/index.nh.shtml>). If the following conditions are satisfied for at least one of the Δ values at one longitude, then the circulation at this longitude is regarded as blocking,

- 1) $\text{GHGS} > 0$,
- 2) $\text{GHGN} < -10 \text{ m}^{\sigma-1}$.

c. MWT, canonical transfer, and localized MS-EVA

The methodology for this study is the localized MS-EVA (Liang and Robinson 2005) [see Liang (2016) for a systematic introduction]. It is based on a new functional analysis tool (MWT; Liang and Anderson 2007), with which one can decompose a function space into a direct sum of orthogonal subspaces, each with an exclusive range of scales, while preserving its local properties. Each subspace is spanned by wavelet bases (can be any orthonormal bases; e.g., Fournier 2002) with the designated scales and is termed a scale window, or simply a window. In this study, we need three-scale windows, a basic-flow window, and a blocking window, plus a window of synoptic eddies. For convenience, write them as $\varpi = 0, 1$, and 2 , respectively. These windows are demarcated on the wavelet spectrum by three ‘‘window bounds’’—that is, three upper-wavelet-scale levels j_0, j_1 , and j_2 . Correspondingly, in the time domain, for a time span τ , the time-scale bounds are $\tau \times 2^{-j_0+1}$, $\tau \times 2^{-j_1+1}$, and $\tau \times 2^{-j_2}$, respectively.

Given a series $u(t)$, take the MWT of u and we obtain two types of quantities: the transform coefficients, $\hat{u}_n^{\sim\varpi}$, and the multiscale window reconstruction (MWR), $u^{\sim\varpi}$ ($\varpi = 0, 1, 2$). MWT and MWR form a transform pair (just as Fourier transform and inverse Fourier transform), but they are distinctly different concepts; the former is defined in phase space while the latter is defined in physical space. MWR functions like a filter and the MWR of $u(t)$, $u^{\sim\varpi}$, is the filtered signal on window ϖ . The MWT has many nice

properties, allowing for a precise representation of multiscale energy as the square of the MWT coefficients (up to some constant). For example, the energy of the blocking-scale window extracted from $u(t)$ is simply $(\hat{u}_n^{\sim 1})^2$ multiplied by some constant. Note it is not $(u^{\sim 1})^2$, which appears in many publications in the literature. Also note that, by adopting a symmetric extension scheme, the transform and reconstruction have a reduced effect from initial and final time values that could influence the interior reconstructed fields (cf. Figs. 10 and 11 in Liang and Anderson 2007).

Application of the MWT to the primitive equations yields the localized multiscale energetics. The multiscale kinetic energy (KE) and available potential energy (APE) equations are, from Liang (2016),

$$\begin{aligned} \frac{\partial K^\varpi}{\partial t} + \underbrace{\nabla \cdot \left[\frac{1}{2} (\widehat{\mathbf{v}\mathbf{v}_h})^{\sim\varpi} \cdot \widehat{\mathbf{v}}_h^{\sim\varpi} \right]}_{\nabla \cdot \mathbf{Q}_K^\varpi} \\ = \frac{1}{2} \underbrace{\left\{ (\widehat{\mathbf{v}\mathbf{v}_h})^{\sim\varpi} : \nabla \widehat{\mathbf{v}}_h^{\sim\varpi} - [\nabla \cdot (\widehat{\mathbf{v}\mathbf{v}_h})^{\sim\varpi}] \cdot \widehat{\mathbf{v}}_h^{\sim\varpi} \right\}}_{\Gamma_K^\varpi} \\ - \underbrace{\nabla \cdot (\widehat{\mathbf{v}}^{\sim\varpi} \widehat{\Phi}^{\sim\varpi})}_{\nabla \cdot \mathbf{Q}_P^\varpi} - \underbrace{\widehat{\omega}^{\sim\varpi} \widehat{\alpha}^{\sim\varpi}}_{b^\varpi} + F_K^\varpi \end{aligned} \quad (1)$$

and

$$\begin{aligned} \frac{\partial A^\varpi}{\partial t} + \underbrace{\nabla \cdot \left[\frac{1}{2} c (\widehat{\mathbf{v}T})^{\sim\varpi} \widehat{T}^{\sim\varpi} \right]}_{\nabla \cdot \mathbf{Q}_A^\varpi} \\ = \frac{c}{2} \underbrace{\left[(\widehat{\mathbf{v}T})^{\sim\varpi} \cdot \nabla \widehat{T}^{\sim\varpi} - \widehat{T}^{\sim\varpi} \nabla \cdot (\widehat{\mathbf{v}T})^{\sim\varpi} \right]}_{\Gamma_A^\varpi} \\ + \underbrace{\widehat{\omega}^{\sim\varpi} \widehat{\alpha}^{\sim\varpi}}_{b^\varpi} + F_A^\varpi, \end{aligned} \quad (2)$$

where K^ϖ and A^ϖ are the KE and APE on window ϖ , respectively, and T is temperature, L lapse rate, L_d the lapse rate for dry air, \mathbf{v} velocity vector, and \mathbf{v}_h its horizontal component. Other symbols are conventional. The explanation of each term is given in Table 1. The colon operator ‘‘:’’ in Eq. (1) is defined such that, for two dyadic products \mathbf{AB} and \mathbf{CD} , $(\mathbf{AB}) : (\mathbf{CD}) = (\mathbf{A} \cdot \mathbf{C})(\mathbf{B} \cdot \mathbf{D})$. Note for simplicity, the dependence on the time step n has been suppressed. Besides, missing from the left-hand side is an artificial term resulting from the time-varying basis, whose inclusion we believe would not change our interpretation of the energetics for $\varpi < 2$. Since here we are concerned only about the blocking window (i.e., $\varpi = 1$), it is omitted. In the other terms, b stands for buoyancy conversion, \mathbf{Q} for flux ($\nabla \cdot \mathbf{Q}$ hence

TABLE 1. Multiscale energetics for the blocking circulation.

| | | |
|-----------------------|--|--|
| K^ϖ | $\frac{1}{2} \hat{\mathbf{v}}_h^{\sim\varpi} \cdot \hat{\mathbf{v}}_h^{\sim\varpi}$ | KE on scale window ϖ |
| \mathbf{Q}_K^ϖ | $\frac{1}{2} (\widehat{\mathbf{v}\mathbf{v}_h})^{\sim\varpi} \cdot \hat{\mathbf{v}}_h^{\sim\varpi}$ | Flux of KE on window ϖ |
| Γ_K^ϖ | $\frac{1}{2} \left\{ (\widehat{\mathbf{v}\mathbf{v}_h})^{\sim\varpi} : \nabla \hat{\mathbf{v}}_h^{\sim\varpi} - [\nabla \cdot (\widehat{\mathbf{v}\mathbf{v}_h})^{\sim\varpi}] \cdot \hat{\mathbf{v}}_h^{\sim\varpi} \right\}$ | Canonical transfer of KE to window ϖ |
| \mathbf{Q}_P^ϖ | $\hat{\mathbf{v}}^{\sim\varpi} \hat{\Phi}^{\sim\varpi}$ | Geopotential flux |
| b^ϖ | $\hat{\omega}^{\sim\varpi} \hat{\alpha}^{\sim\varpi}$ | Buoyancy conversion |
| A^ϖ | $\frac{1}{2} c (\hat{T}^{\sim\varpi})^2, c = \frac{g}{\overline{T}(g/c_p - L)}$ | APE on scale window ϖ |
| \mathbf{Q}_A^ϖ | $\frac{1}{2} c \hat{T}^{\sim\varpi} (\widehat{\mathbf{v}T})^{\sim\varpi}$ | Flux of APE on window ϖ |
| Γ_A^ϖ | $\frac{c}{2} \left[(\widehat{\mathbf{v}T})^{\sim\varpi} \cdot \nabla \hat{T}^{\sim\varpi} - \hat{T}^{\sim\varpi} \nabla \cdot (\widehat{\mathbf{v}T})^{\sim\varpi} \right]$ | Canonical transfer of APE to window ϖ |

represents a transport process), F for dissipation–diffusion processes, and Γ for transfer of energy to window ϖ from other windows. The subscripts K and A stand for KE and APE, respectively; hence, $\nabla \cdot \mathbf{Q}_K^\varpi$ and $\nabla \cdot \mathbf{Q}_A^\varpi$ mean the divergence of the KE and APE fluxes. The other divergence term, $\nabla \cdot \mathbf{Q}_P^\varpi$, means the work done by the pressure gradient force. Among these energetics, the transports and transfers are derived from the nonlinear advection terms in the original governing equations.

One thing that should be mentioned is with the transfer (Γ terms) and transport ($\nabla \cdot \mathbf{Q}$ terms) processes. Their separation from the nonlinear terms is very important for this study, since it is directly related to the blocking evolution. This kind of transfer possesses a very interesting property, namely,

$$\sum_{\varpi} \sum_n \Gamma_n^\varpi = 0 \tag{3}$$

as proved in Liang (2016, section 3). Physically this means that the transfer is a mere redistribution of energy among the scale windows, without generating or destroying energy as a whole. This property, though simple to state, is not met in previous time decomposition-based or statistical energetic formalisms. To distinguish it from those which one may have encountered in the literature, the above transfer is termed *canonical transfer*.

Note that all the energetic terms in Eqs. (1) and (2) are localized both in space and in time; in other words, they are all four-dimensional field variables, distinguished notably from the classical Reynolds decomposition or Fourier analysis-based formalisms in which localization is lost in at least one dimension of space–time to achieve the scale decomposition. Processes localized in space and time are thus naturally embedded here. A schematic of the energy flow is shown in Fig. 1.

In Eqs. (1) and (2), the canonical transfer terms are Γ_K^ϖ and Γ_A^ϖ . It has been established that they correspond

precisely to two important geophysical fluid flow processes—that is, the barotropic instability and baroclinic instability (Liang and Robinson 2007). If only the basic-flow and blocking windows are considered, then

- 1) a flow is locally unstable if $\Gamma_K^1 + \Gamma_A^1 > 0$, and vice versa;
- 2) for an unstable system, if $\Gamma_K^1 > 0$ and $\Gamma_A^1 \leq 0$, the instability that the system undergoes is barotropic;
- 3) for an unstable system, if $\Gamma_A^1 > 0$ and $\Gamma_K^1 \leq 0$, then the instability is baroclinic; and
- 4) if both Γ_A^1 and Γ_K^1 are positive, the system is experiencing a mixed instability.

3. Blocking composition and multiscale geopotential reconstruction

a. Blocking composition

Considering that a blocking must be stationary at one longitude and extend to a relatively large region, only the episodes that meet the TM index criterion in at least a longitudinal range of 12.5°, as suggested by Barriopedro et al. (2006), and simultaneously last for more than 4 days (Tibaldi and Molteni 1990; Pelly and Hoskins 2003), are regarded as blocking. The blocking characteristics change with season, and Barriopedro et al. (2006) find that the long-lasting blocking episodes with larger extension and intensity prevail in winter over the ocean. So only the events occurring in December, January, and February (DJF) are analyzed in this study. The result is shown in Fig. 2, from which we see that most blocking episodes (45 in total) exist at 7.5°W; it is found that the mechanisms controlling the blockings are different for different longitudes; we hence only focus on this longitude for the composition.

Since GHGS and GSGN are the geopotential height gradients of a blocking in its southern part and northern

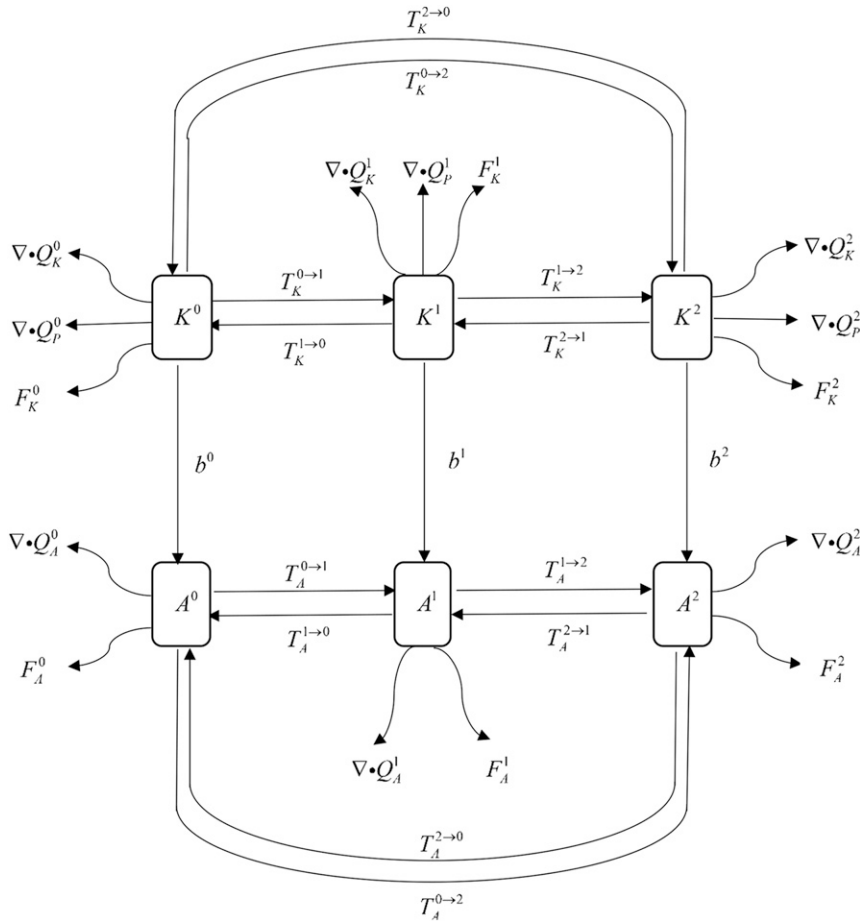


FIG. 1. The energy processes in a three-scale window decomposition. The numbers 0, 1, and 2 indicate the basic-flow window, blocking window, and synoptic window, respectively. The symbols are referred to in Table 1.

part, the difference of these two can be used to measure the blocking strength. With this, we pick the strongest day of every blocking episode, average the geopotential on all the strongest days, and take the average as the composite geopotential for blocking day 0. Likewise, we may obtain the composite geopotential for blocking day . . . , -6, -4, 0, 4, 6, The output of the composition is shown in Fig. 3. It is clear that the blocking commences on day -4, intensifies on day -2, culminates on day 0, and weakens and decays on days 2 and 4. This is the typical omega-type blocking. The stationary feature is also clear, as the center of the high almost stays in the same region during the evolution. The composite blocking lasts about 10 days, consistent with the typical lifetime.

b. Multiscale window reconstruction of the 300-hPa geopotential field

As shown by Sawyer (1970), the maximum amplitude of the 15–60-day low-frequency disturbances corresponds

well with the preferred location of blocking. We hence focus on the 8–64-day scale to include this scale range, or scale window, and exclude synoptic eddies with typical lifetime less than about one week in this study. We use the MWT developed by Liang and Anderson (2007) to reconstruct the geopotential on three different scale windows—namely, a basic-flow window containing scales above 64 days, a blocking window containing scales from 8 to 64 days, and a synoptic window with eddies of scales less than 8 days.

With the filtered fields, we repeat the composition as in the preceding section. The composite basic-flow-scale and blocking-scale geopotential are shown in Figs. 4a and 4b. The basic flow shows as a ridge with a southwest–northeast tilting; it does not change much with time. On the blocking scale, a clear high cell is found and it propagates westward during the period. As the basic flow rarely varies and the synoptic eddies have small magnitudes, we can safely say that it is the blocking-scale window that contributes most to the geopotential

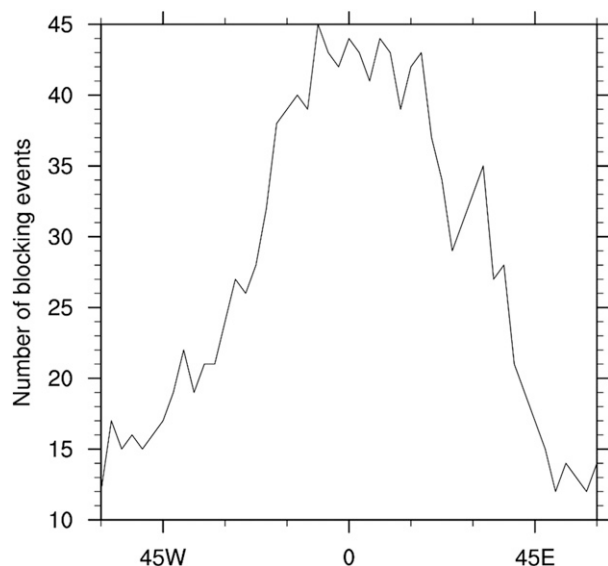


FIG. 2. Number of blocking episodes during the study period vs longitude.

variability during the blocking. We hence focus on the analysis on this scale window.

The high cell on the blocking-scale window originates on day -12 over middle Eurasia, with a center at about 60° – 110° E. After generation, it propagates westward, as is clear in the Hovmöller diagram of the 300-hPa geopotential on the blocking window (Fig. 4c). Overall, the lifetime of this high cell is about 24 days. A similar signal has also been identified over Euro-Atlantic by Michelangeli and Vautard (1998) through compositing the truncated planetary-scale anomalies before the onset of blocking and over North Pacific by Kushnir (1987) and Branstator (1987) through projecting the geopotential into its first principal component.

4. Energetics of the blocking signal

Kushnir (1987) investigates the evolution of the spatially averaged energy (over half of the Northern Hemisphere) of the 10–40-day wintertime low-frequency disturbances over Pacific Ocean. While it has led to understanding of the phenomenon, atmospheric blockings are local and on the move, which is beyond the capability of a spatially averaged analysis methodology. In this study, the MS-EVA is utilized to approach the problem. As introduced previously, MS-EVA will yield the multiscale energetics in a 4D fashion. We then track the high-pressure center and integrate the energetics around the center. Shown in the following are the deviations of the energy budget terms from their wintertime means (averaged over December–February during the periods of 1957–2002; the mean part is referred to in the appendix),

considering that the high pressure cell is only one part of the signal on the 8–64-day window, and that the effect of other parts should be taken out. Kushnir (1987) adopts a similar procedure; he takes deviations of energy budget terms from their 10-yr means. Statistical significance should be tested for the obtained composite energetics. This turns out to be difficult, as the ensemble is small. Nonetheless, Fournier (2003) manages to develop a practical method to tackle the problem. We hence follow his approach to fulfill the test. Note in the following, when we say a value is “significant,” we mean “it is significant by the standard set in Fournier (2003)”; it may be different from the significance test in the usual sense.

a. KE evolution

To see how the blocking as a whole evolves, we average the KE energetics over the blocking region. It is found that the blocking-scale KE is almost located in the regions with positive blocking-scale geopotential (Fig. 5a presents such an example); the integration/averaging of the energetics is hence over a domain with the positive composite Φ^{-1} (i.e., $\Phi^{-1} \geq 0 \text{ m}^2 \text{ s}^{-2}$) throughout all the pressure levels. But, note that these regions may involve some processes other than the blocking. This is fixed by excluding the regions west of 30° E during the onset phase and those east of 30° E during the decay phase. The averaging domains defined by other standards ($\Phi^{-1} \geq 100 \text{ m}^2 \text{ s}^{-2}$ and $\Phi^{-1} \geq 200 \text{ m}^2 \text{ s}^{-2}$) have also been used to test the sensitivity of energetics calculation. The outcome (not shown) is not sensitive to the choice of averaging region domain. From Fig. 5b, the KE of the high cell begins to increase from blocking day -8 , maximizes on day 0, then becomes on decline. Obviously, during the KE evolution, the energy balance varies. In the beginning, the system mainly gains KE from the pressure work ($-\nabla \cdot \mathbf{Q}_p^1$); then the KE transfer from the synoptic window ($\Gamma_K^{2 \rightarrow 1}$) dominates the balance, agreeing with the theoretical study of Jin et al. (2006); and then the energy transport ($-\nabla \cdot \mathbf{Q}_K^1$) and buoyancy conversion ($-b^1$) collaborate to cause KE to decay. For analysis convenience, we will hence forth define the period from day -12 through day -8 as the onset phase, that from day -8 through day 0 as the amplification phase, and that from day 0 through day 8 as the decay phase. In the following we analyze the energetics during the three phases one by one. The time-mean energy processes during these phases are shown in Fig. 6.

1) ONSET PHASE

In the onset phase, most of the KE comes from pressure work (Figs. 5b and 6a). Its time-mean zonal section distribution is shown in Fig. 7a. Positive pressure work occupies most of the central part of the high-pressure cell.

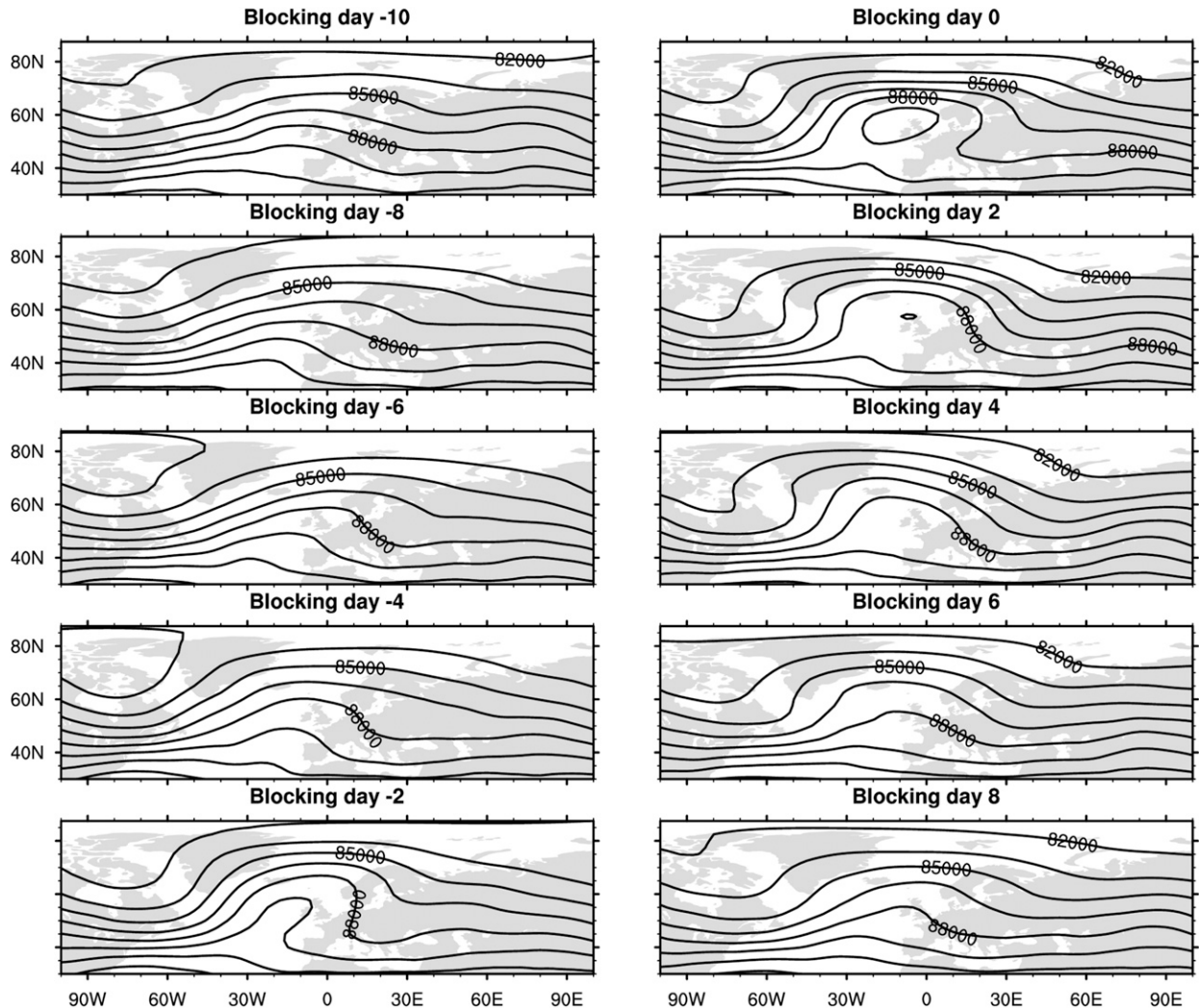


FIG. 3. The composite blocking over the Atlantic from (top left to bottom right) day -10 to day 8 . Contoured is the geopotential ($\text{m}^2 \text{s}^{-2}$) at 300 hPa .

The secondary contribution in this phase is the canonical transfer from the synoptic eddies (Figs. 5b and 6a); shown in Fig. 7b is its distribution. An observation is that canonical transfer from the synoptic scale takes effect mainly between 500 and 200 hPa , while pressure work exists through almost all the levels. In the interior of the cell, pressure work plays the major role; on the western and eastern sides, canonical transfer from the synoptic scale contributes positively to the blocking. Obviously, the two processes play a vital role in blocking onset.

2) AMPLIFICATION PHASE

After the onset, the KE keeps increasing, particularly from day -4 to day 0 . The KE budget in Fig. 5b clearly tells that the canonical KE transfer dominates this period; next to it are KE transport and pressure work (Fig. 5b). The spatial distribution of the canonical KE transfer from

day -4 to day 0 is displayed in Fig. 8a; also displayed is the KE transport and pressure work (Figs. 8b and 8c). These processes are most active through 500 – 200 hPa . From the figure, the KE transfer from the synoptic-scale window takes place around 50° – 25°W and 10°W – 60°E , which are both positive. In contrast, the KE transport on the blocking-scale window can be positive and negative, with the positive center around 25°W – 10°E and the negative center around 50° – 25°W . For pressure work, it is essentially negative through the region 25°W – 60°E . We hence have the following KE energetic scenario on the blocking window: on the western side of the high-pressure cell, the positive canonical transfer from the synoptic window is mainly balanced by a negative KE transport, while on the eastern side of and within the cell, the balance is between the canonical transfer, the KE transport, and the pressure work.

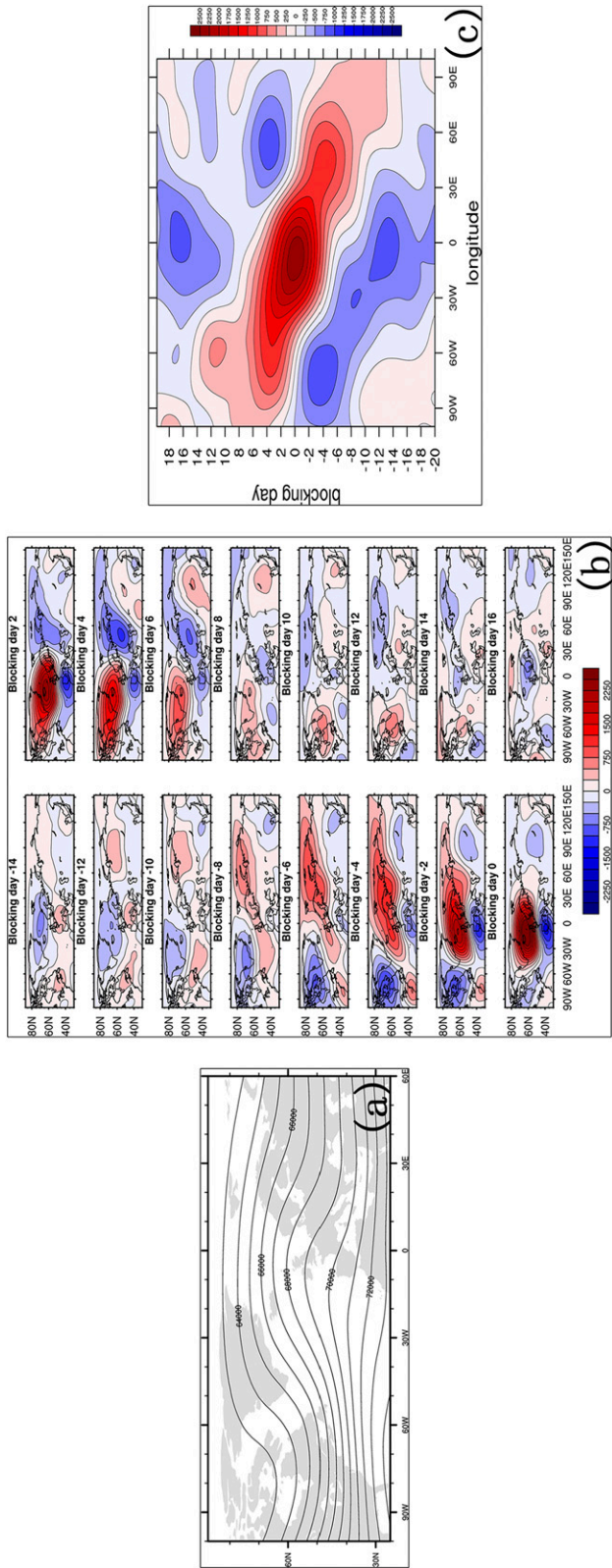


FIG. 4. The composite 300-hPa geopotential on (a) the basic-flow-scale window and (b) the blocking-scale window from day -14 to day 16 ($m^2 s^{-2}$), and (c) the Hovmöller diagram of the above-blocking-scale geopotential at 60°N.

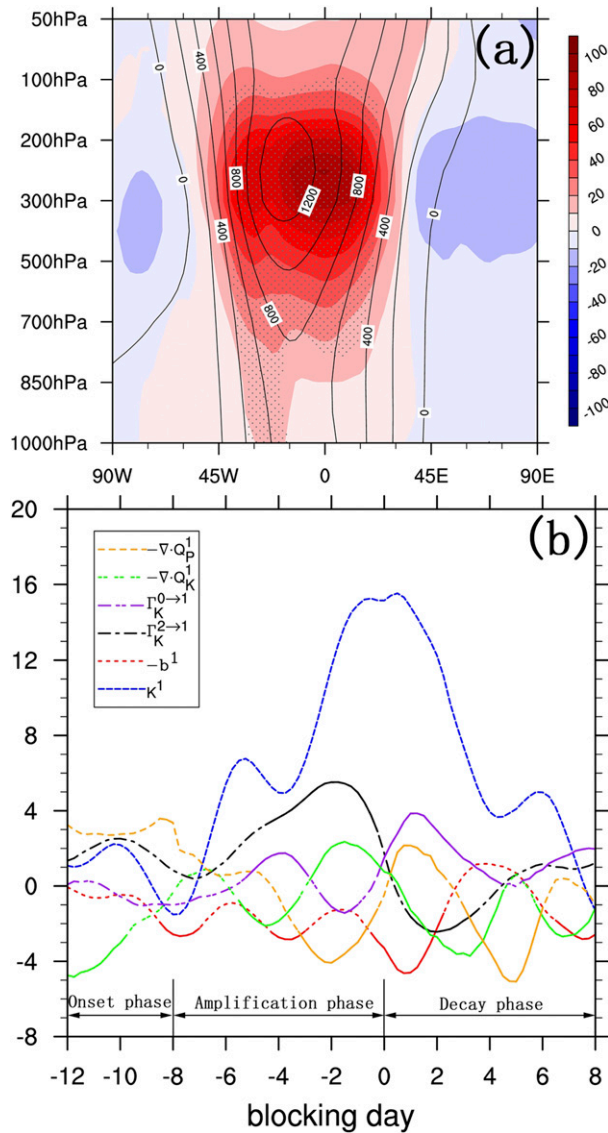


FIG. 5. (a) The blocking-scale KE (color shaded; $\text{m}^2 \text{s}^{-2}$) and geopotential (contoured; $\text{m}^2 \text{s}^{-2}$) on day 0 averaged over $45^\circ\text{--}80^\circ\text{N}$. (b) Evolution of the blocking-scale KE ($\text{m}^2 \text{s}^{-2}$) and KE energetics ($10^{-5} \text{m}^2 \text{s}^{-3}$) averaged over the blocking high pressure cell: $-\nabla \cdot \mathbf{Q}_p^1$ (orange), $-\nabla \cdot \mathbf{Q}_k^1$ (green), $\Gamma_K^{0 \rightarrow 1}$ (purple), $\Gamma_K^{2 \rightarrow 1}$ (black), $-b^1$ (red) and K^1 (blue). (a) The hatched parts and (b) the solid segments denote the parts significant by the standard set by Fournier (2003).

3) DECAY PHASE

In Fig. 4b, we observe a fast retrograding process of the signal in the decay phase after day 0. The center lies at around 7.5°W on day 0 and moves to 75°W on day 10. The evolution of the kinetic energetics shows that the development during this period is mainly governed by KE transport and buoyancy conversion (Figs. 5b and 6c). So we draw the meridionally averaged (over $45^\circ\text{--}80^\circ\text{N}$) time-mean vertical-longitudinal distribution of these two terms

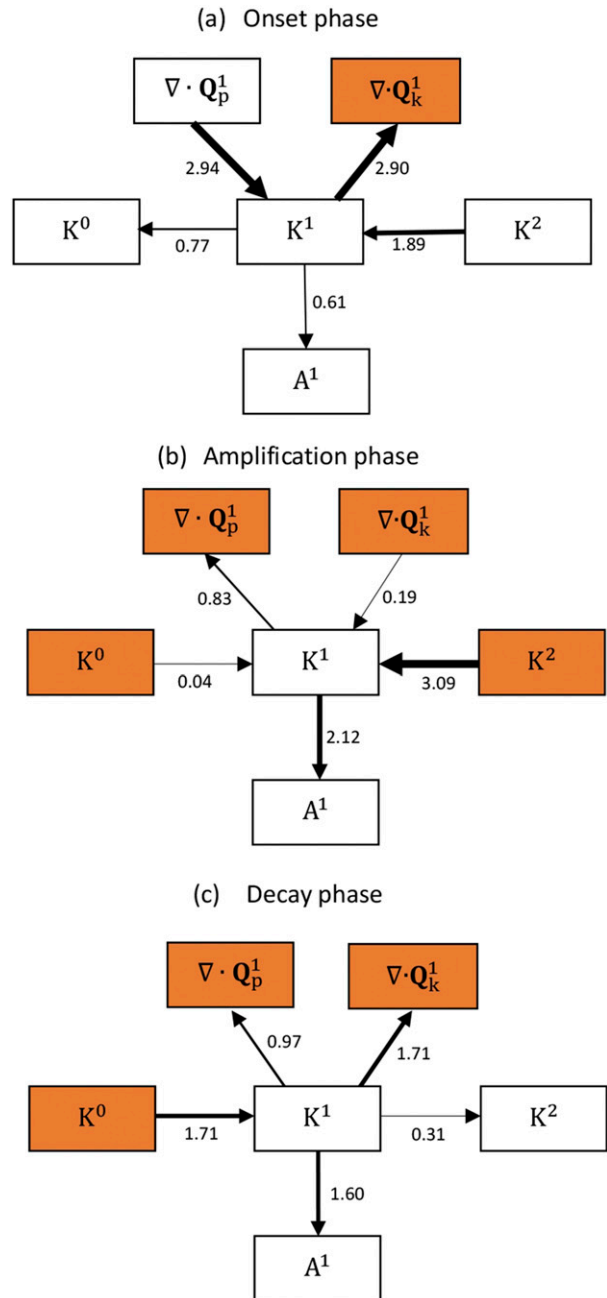


FIG. 6. Energetics averaged over the three distinct phases: (a) onset, (b) amplification, and (c) decay. The thickness of the arrows is proportional to the magnitude of every term ($10^{-5} \text{m}^2 \text{s}^{-3}$). The superscripts 0, 1, and 2 represent the basic-flow, blocking, and synoptic windows. The orange shading means that the corresponding term is significant by Fournier’s test.

in Fig. 9. The negative contributions of KE transport and buoyancy conversion are evident. The pattern not only tells that the KE transport weakens the cell but also implies that it may account for the cell’s retrograding. At the eastern edge, the KE transport is positive, while on the

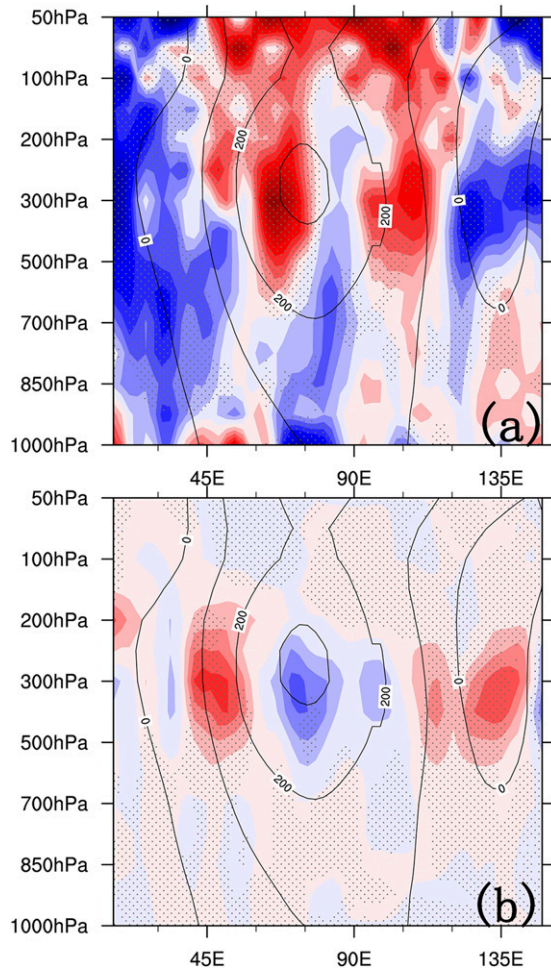


FIG. 7. (a) Time-mean (over the onset phase) zonal–vertical sectional distribution of the blocking-scale pressure work rate $-\nabla \cdot \mathbf{Q}_p^1$ (color shaded, $10^{-4} \text{ m}^2 \text{ s}^{-3}$) and geopotential (contoured, $\text{m}^2 \text{ s}^{-2}$) averaged over $45^\circ\text{--}80^\circ\text{N}$. (b) As in (a), but the shaded regions are for canonical KE transfer from the synoptic window $\Gamma_K^{2 \rightarrow 1}$ ($10^{-4} \text{ m}^2 \text{ s}^{-3}$). Dotted are the regions significant by Fournier's test.

western side it is negative. This makes the wind stronger in the east and weaker in the west. The wind in the east is southward; its sudden acceleration leads to an imbalance in geostrophy and hence a surplus of westward force due to the Coriolis effect. Likewise, the sudden deceleration of the wind in the west results in a surplus of westward pressure gradient. Both effects may give rise to a westward migration of the system.

b. APE evolution

An interesting phenomenon is that, during the blocking, temperature is abnormally high (e.g., Green 1977); it is hence necessary to check the APE evolution. We find that the APE related to this temperature anomaly concentrates beneath 300 hPa and in the region enclosed

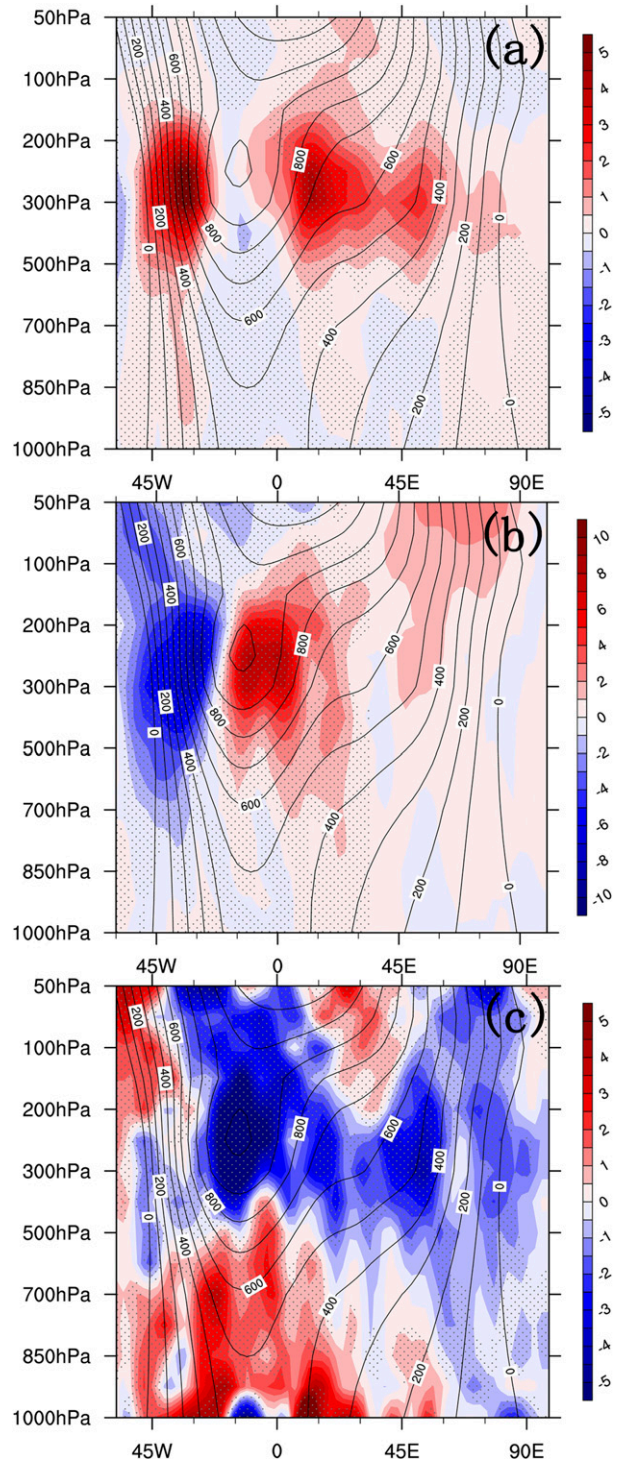


FIG. 8. As in Fig. 7, except that the color shading represents (a) the canonical transfer from the synoptic-scale window to the blocking window ($\Gamma_K^{2 \rightarrow 1}$), (b) the KE transport on the blocking window ($-\nabla \cdot \mathbf{Q}_K^1$), and (c) the blocking-scale pressure work ($-\nabla \cdot \mathbf{Q}_p^1$) over the period from day -4 to day 0 . The color scale in (a) and (c) runs from -5 to $5 \times 10^{-4} \text{ m}^2 \text{ s}^{-3}$ in increments of $1 \times 10^{-4} \text{ m}^2 \text{ s}^{-3}$ and in (b) from -10 to $10 \times 10^{-4} \text{ m}^2 \text{ s}^{-3}$ in increments of $2 \times 10^{-4} \text{ m}^2 \text{ s}^{-3}$.

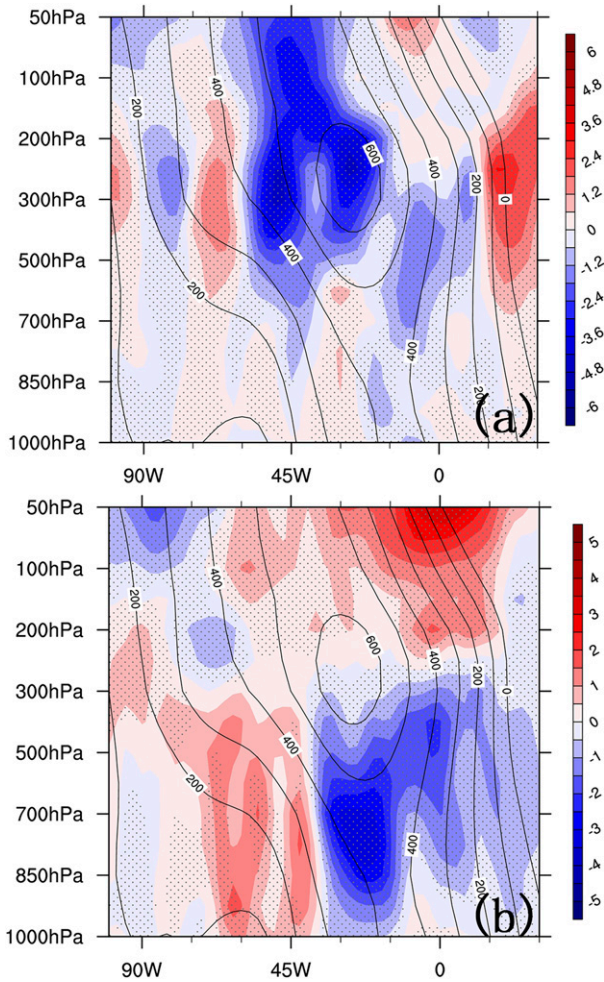


FIG. 9. As in Fig. 7, but the shading is (a) KE transport ($-\nabla \cdot \mathbf{Q}_K^1$) and (b) buoyancy conversion ($-b^1$) on the blocking-scale window over the decay phase.

by the $200 \text{ m}^2 \text{ s}^{-2}$ geopotential isoline on the blocking window (e.g., Fig. 10a). We choose this domain ($\Phi^{-1} \geq 200 \text{ m}^2 \text{ s}^{-2}$, 1000–300 hPa) to average the energetics. Averaging over other domains (e.g., $\Phi^{-1} \geq 300 \text{ m}^2 \text{ s}^{-2}$ and $\Phi^{-1} \geq 400 \text{ m}^2 \text{ s}^{-2}$) have also been done and the results (not shown) are similar. From Fig. 10b, the APE evolution experiences two phases, each corresponding to a maximum. In the first phase, it is mainly governed by the APE transfer from the basic-flow window to the blocking window ($\Gamma_A^{0 \rightarrow 1}$) (i.e., governed by a baroclinic instability), while in the second phase it is dominated by buoyancy conversion (b^1). Instability similar to that in the first maximum has been found in the west Pacific teleconnection pattern (e.g., Tanaka et al. 2016) and in a sudden stratospheric warming episode (Xu and Liang 2017). These phases are roughly from day -9 to day -3 and from day -3 to day 4 , respectively. The energy processes in these two phases are diagrammatized in

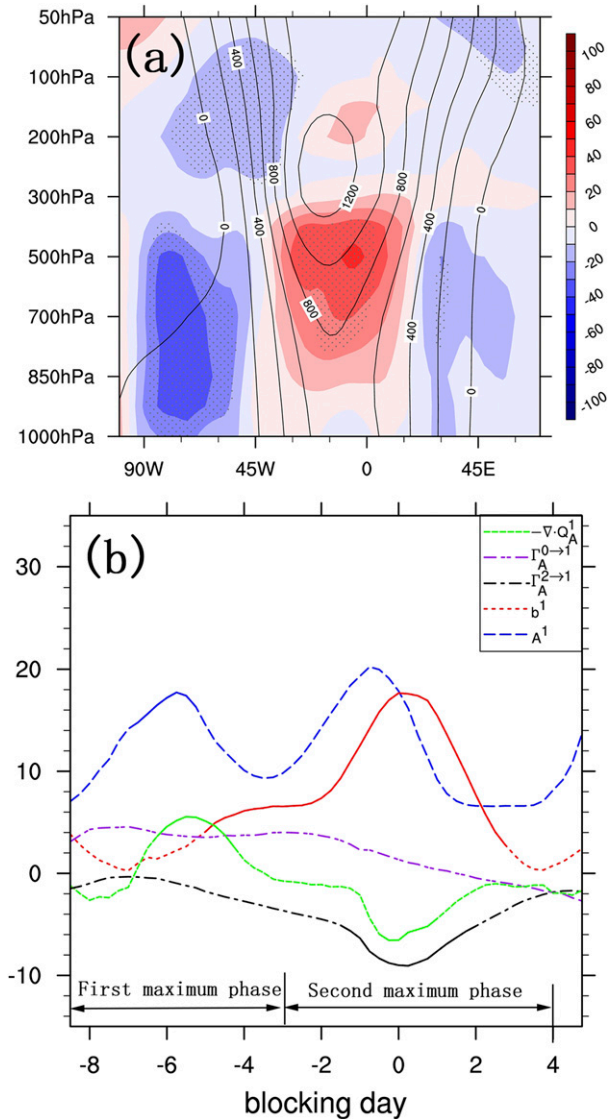


FIG. 10. As in Fig. 5, but for the blocking-scale APE ($\text{m}^2 \text{ s}^{-2}$) and APE energetics ($10^{-5} \text{ m}^2 \text{ s}^{-3}$) for the high-pressure cell. Refer to the text for the averaging domain.

Fig. 11 with the numbers quantitatively showing the contribution of the designated terms. In the following, we elaborate on these phases separately.

1) FIRST MAXIMUM PHASE

The zonal–vertical distribution of the canonical APE transfer from the basic flow is shown in Fig. 12a. Clearly, this transfer occupies most of the lower region of the high-pressure cell. Because of its relation to heat transfer, it will give rise to temperature anomaly, which we draw in Fig. 12b. The positive temperature anomaly is obvious in the lower region. This agrees with the observation that a blocking usually has a warm core in the troposphere. According to Liang and Robinson (2007),

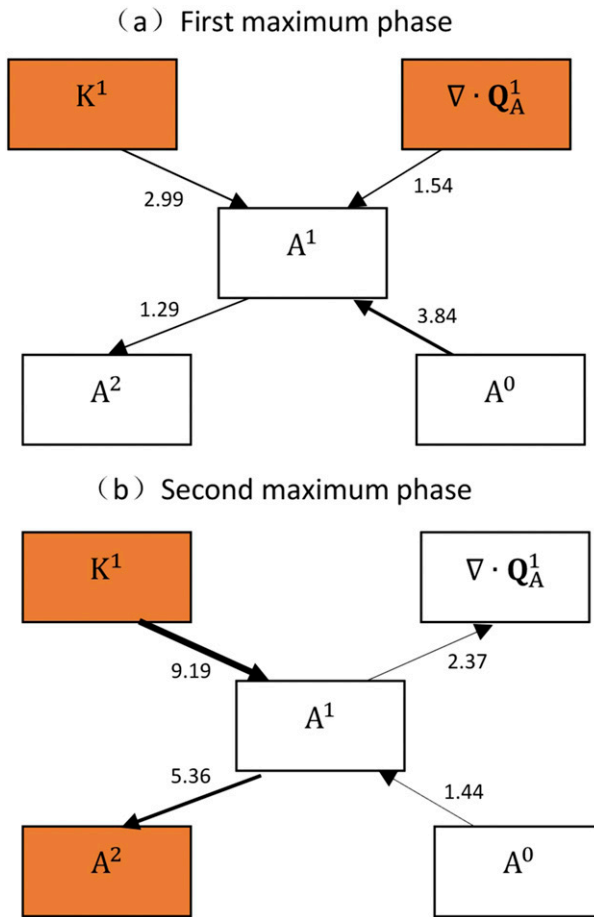


FIG. 11. As in Fig. 6, but for the blocking-scale APE energetics for the two phases.

$\Gamma_A^{0 \rightarrow 1}$ implies a baroclinic instability. So, in this phase, during this period the warm anomaly in the troposphere is maintained by a baroclinic instability.

2) SECOND MAXIMUM PHASE

In this phase, buoyancy conversion dominates the APE balance. Figure 13a is the vertical–longitudinal section distribution of the buoyancy conversion, which occupies most of the lower region of the cell. By definition, a positive buoyancy conversion means a loss of KE to APE. This implies warm air downward or cold air upward. To see this, we draw the vertical velocity ω in Fig. 13b. Clearly, in the region of the positive buoyancy conversion ω directs downward. A direct result is that the high-pressure cell in the troposphere must be warmer than the environment, which is indeed true (shown in Fig. 13c). Green (1977) suggests that the formation of blocking warm high is due to the descending of dry air from upper levels. Our analysis is consistent with this. So, in this phase, the warm core is maintained by the buoyancy conversion from the kinetic energy within the blocking window.

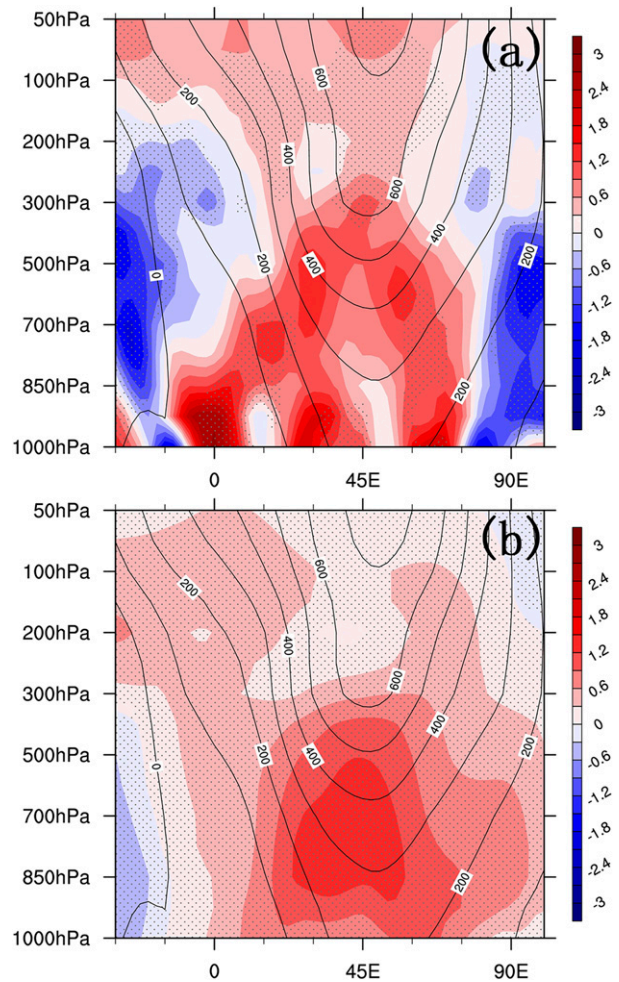


FIG. 12. (a) As in Fig. 7, except that the shading is the canonical APE transfer from the basic flow to the blocking ($\Gamma_K^{0 \rightarrow 1}$) in the first maximum phase. (b) As in (a), but the shading is the blocking-scale temperature (K).

5. Energetics on other scale windows

As is shown in Fig. 4b, the blocking high pressure cell is most active in the region 40°N–80°N, 45°W–45°E. We hence examine large-scale and synoptic-scale energetics averaged over this domain and throughout the vertical levels from day –12 to day 8. Shown in Figs. 14 and 15 are the averaged energetics departures from their respective time means; the means are referred to the appendix. By calculation, KE and APE are decreasing on both windows in this region. On the basic-flow window, as we know, the westerly is blocked when blocking occurs. This is why the large-scale KE is reduced, and indeed, the energetics show that the KE transport process is the most important factor. For APE, the buoyancy conversion accounts for its reduction. On the synoptic window, as shown in Fig. 15, KE is reduced mainly owing to the KE

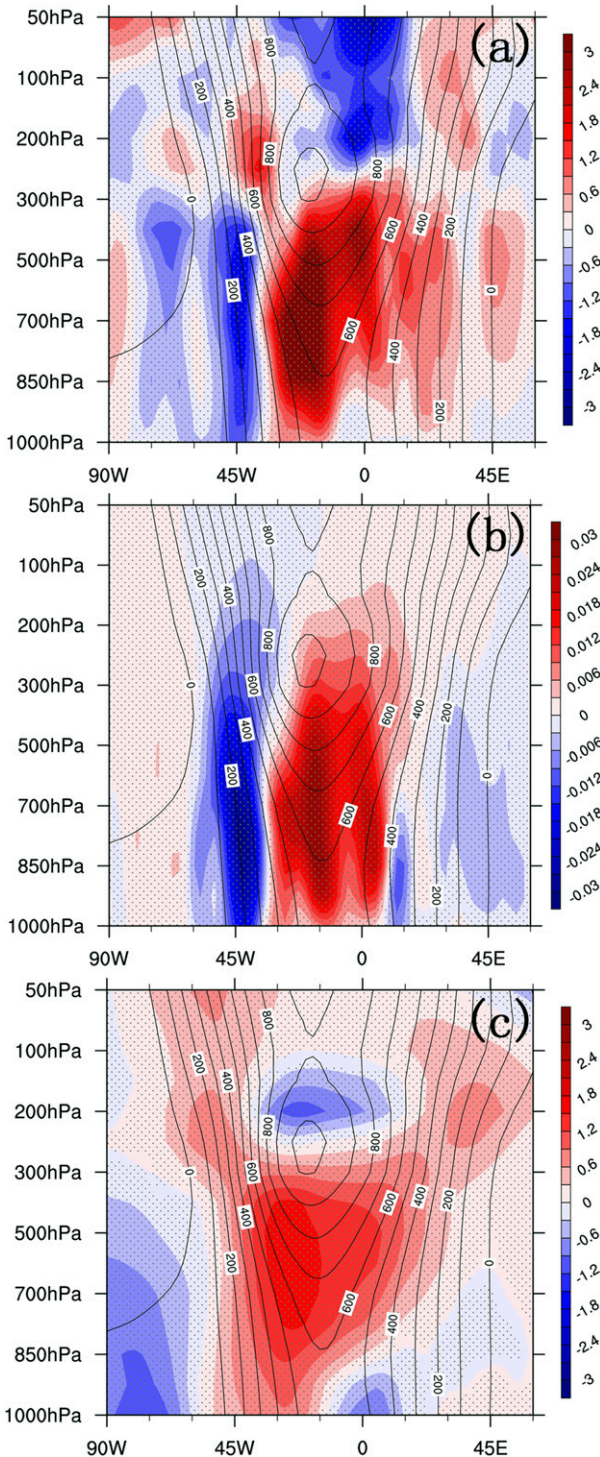


FIG. 13. (a) As in Fig. 7, except that the shading is the conversion ($-b^1$) from KE to APE in the second maximum phase. (b) As in (a), but the shading is vertical velocity (Pa s^{-1}). (c) As in (a), but the shading is temperature (K).

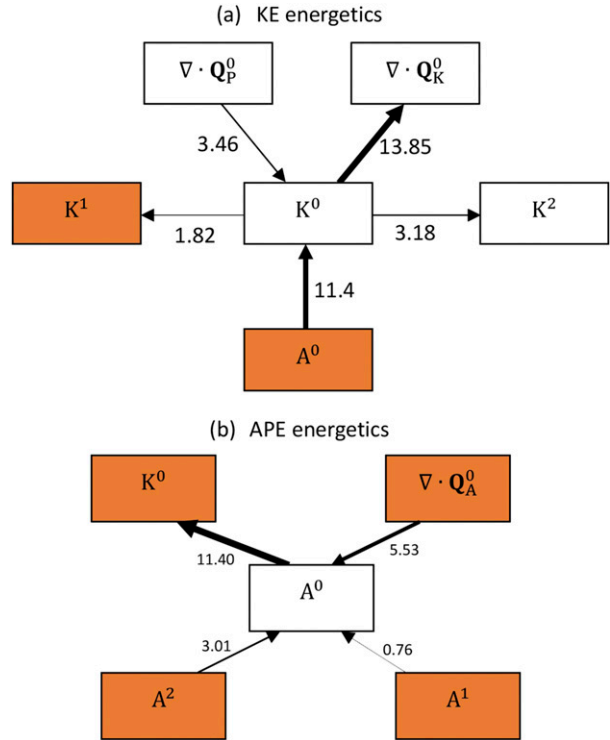


FIG. 14. Basic-flow energetics (with time mean removed) averaged from day -12 to day 8 over the region 40°N – 80°N , 45°W – 45°E throughout all vertical levels. The arrow thickness is proportional to the magnitude ($10^{-5} \text{ m}^2 \text{ s}^{-3}$). The shaded boxes are the statistically significant terms.

canonical transfer from the synoptic-scale window to the blocking-scale window, in agreement with the analysis in section 4a(2). Similarly, the upscale APE canonical transfer from the synoptic-scale window to basic-flow window causes the synoptic APE reduction.

6. Discussion

The KE transfer from the synoptic-scale window is almost in phase with the high pressure cell on the blocking-scale window (Fig. 8a). This is in agreement with Robinson (1991), who shows in his theoretical study that the high-frequency forcing to wave 1 is more in phase with the low-frequency streamfunction, considering that the signal we discuss is almost of zonal wavenumber 1 (Fig. 4b). However, earlier on, Illari (1984) and Mullen (1987) find a quadrature phase relation between the eddy forcing and blocking. We note that the different meanings of “eddy forcing” between theirs and ours may account for this inconsistency. The eddy forcing in those previous studies is represented by a quadratic term in the vorticity equation, while here we are talking about energetics, with the terms involving the products of three perturbation fields (cf. Table 1). So, the eddy forcing in our study and that in

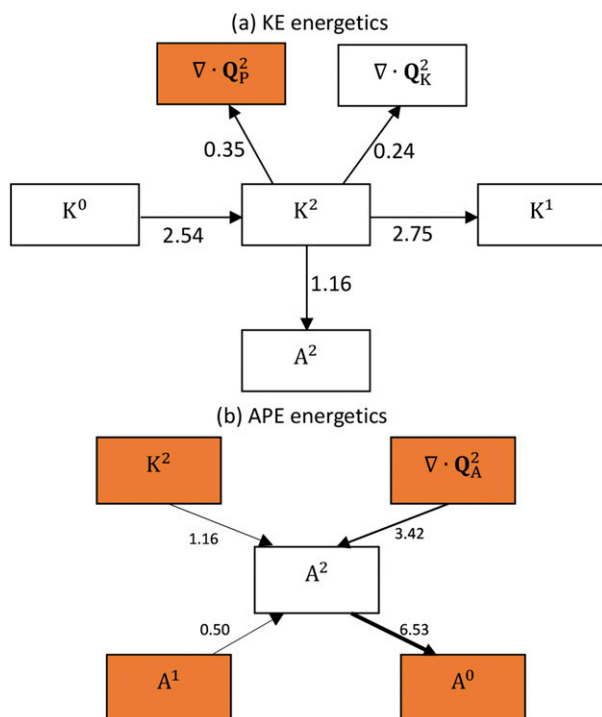


FIG. 15. As in Fig. 14, but for the synoptic-scale window.

theirs mean different things. In this sense, the canonical transfers should not be compared to the previously discussed eddy forcings. Actually, in some previous studies people already report possibly different relations. Except the study of Robinson (1991) mentioned above, Tsou and Smith (1990) find that, though the eddy forcing of synoptic-scale transients is one-quarter wavelength upstream of the blocking, the interaction between planetary and synoptic scales shows an in-phase relation with the blocking (cf. their Fig. 13). A related discussion based on PV flux diagnosis is referred to Arai and Mukougawa (2002).

7. Conclusions

Previously, the low-frequency disturbances and atmospheric blocking have been shown to be closely related (e.g., Namias 1947; Sawyer 1970; Michelangeli and Vautard 1998; Woollings et al. 2008); we hence investigate the dynamics on this range of scales in the hope of gaining an understanding of the blocking processes. For convenience, the scale range, or scale window as it is called, is termed the blocking-scale window. The scale windows above and below are for the synoptic eddies and lower variabilities and are called synoptic window and basic-flow window, respectively. Using a newly developed machinery—namely, multiscale window transform—we decompose the atmospheric fields over Atlantic into variabilities on the three windows and reconstruct the

blocking process through compositing with the index proposed by Tibaldi and Molteni (1990) all the blocking episodes in winter (DJF) from September 1957 to May 2002. From the result, the blocking originates over Europe and behaves as a westward-retrograding signal. When the high-pressure cell starts to move toward the basic-flow ridge but still with a distance, blocking begins to emerge. When the cell travels over the basic-flow ridge, blocking develops, and decays when the cell leaves the ridge behind. This study diagnoses the dynamical processes that underlie the generation, development, and decay of the cell.

The highly localized nature and, particularly, the moving structure of the blocking requires a diagnostic methodology capable of handling processes that are highly nonlinear, multiscale interactive, and localized in space and time. The multiscale energy and vorticity analysis (MS-EVA) developed by Liang and Robinson (see Liang 2016) and the MS-EVA-based instability theory make such a methodology. Application of it reveals that, during different periods, the evolution of the high-pressure cell is controlled by different mechanisms. In the beginning, the KE balance is dominated by pressure work. In the amplification phase, the canonical KE transfer to the blocking window from the synoptic window is the major mechanism. In the decay phase, the KE transport and the buoyancy conversion from KE to APE on the blocking window are the key factors, where the former may account for the fast moving of the disturbances during this period.

For the APE evolution, two phases may be distinguished: namely, the first maximum phase and the second maximum phase. In the first maximum phase, the APE evolution is dominated by canonical APE transfer from the basic flow to the blocking—namely, baroclinic instability according to the theory of Liang and Robinson (2007). In the second maximum phase, the buoyancy conversion from KE to APE on the blocking window is the most important factor. The vertical motion suggests that the buoyancy conversion is caused by the downward motion of warm air, in agreement with the hypothesis proposed by Green (1977). The baroclinic instability and the buoyancy conversion make the warm core for the blocking center.

All in all, the blocking is initiated collaboratively by the pressure work and the upscale canonical transfer from the synoptic eddies, but its further growth and decay are due to the upscale canonical transfer, KE transport within the blocking window, and the buoyancy conversion from KE to APE. This stage dependence of dynamical processes has already been observed in other phenomena, such as sudden stratospheric warming (Xu and Liang 2017). The corresponding warm core in the troposphere also has different maintaining mechanisms. In early times, it is maintained by a baroclinic instability, but in later times,

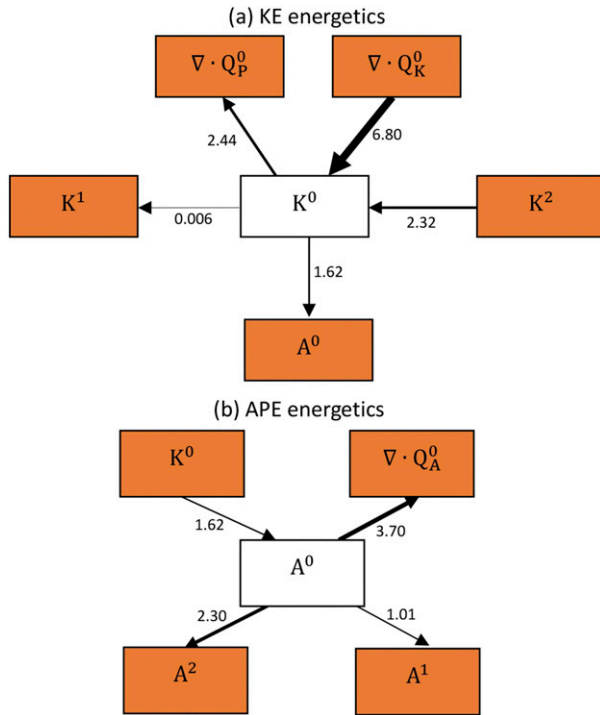


FIG. A1. Time-mean energetics for the basic flow averaged over the region 40°N–80°N, 45°W–45°E through all the vertical levels. The arrow thickness is proportional to the magnitude ($10^{-4} \text{ m}^2 \text{ s}^{-3}$). The shaded boxes are the statistically significant terms.

the mechanism becomes the buoyancy conversion from the blocking-scale KE.

Acknowledgments. We are grateful to Aimé Fournier for important scientific discussions. Thanks are also due to an anonymous referee whose advice helped improve the manuscript. We are indebted to ECMWF for providing the ERA-40 data. Jiwang Ma thanks Yang Yang, Yuanbin Zhao, and Cheng Gong for many valuable discussions. The MS-EVA software can be downloaded (from <http://www.ncoads.org>). This work was partially supported by the National Science Foundation of China (NSFC) under Grant 41276032, by the Jiangsu Provincial Government through the Jiangsu Chair Professorship to XSL and the 2015 Jiangsu Program of Entrepreneurship and Innovation Group, and by the State Oceanic Administration through the National Program on Global Change and Air-Sea Interaction (GASI-IPOVAI-06).

APPENDIX

Climatology of the Multiscale Energetics

Figures A1, A2, and A3 display the time-mean energetic cycles on the three-scale windows, respectively.

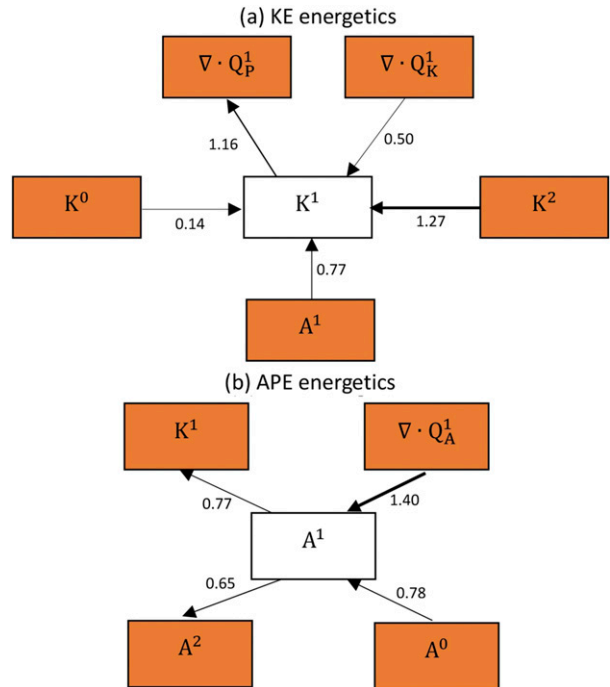


FIG. A2. As in Fig. A1, but for the blocking-scale window.

The time mean is over all the wintertime of the data, and the spatial averaging is over 40°N–80°N, 45°W–45°E throughout all the vertical levels. Shaded are the terms significant by the significance test by Fournier (2003).

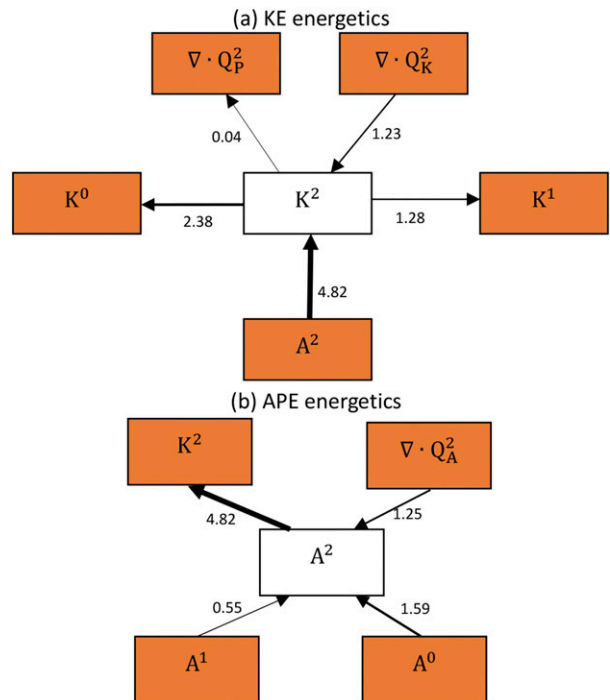


FIG. A3. As in Fig. A1, but for the synoptic-scale window.

On the basic-flow window, obviously, the KE transported from other regions dominates the KE balance (Fig. A1a), while the internal processes in the atmosphere form a sink for the APE (Fig. A1b). On the blocking window, the upscale KE canonical transfer makes the most important source of the KE (Fig. A2a), but the APE is mainly gained through the transport processes (Fig. A2b). For the synoptic eddies, they gain KE mainly through the conversion from APE (Fig. A3a), while part of the APE is supplied from the basic flow through baroclinic instability and through transport from outside (Fig. A3b).

Comparing Figs. A1, A2, and A3, the scale interaction pathways are now clear. The basic-flow transfers APE to synoptic-scale eddies; and on the synoptic-scale window, APE is converted to KE; then, the synoptic-scale KE is transferred upscale to the basic-flow window and blocking-scale window. A similar diagram has been proposed in previous studies (e.g., Oort 1964) in a framework of mean-eddy decomposition. But their studies are conducted over a global domain and, hence, do not have local information and do not involve those mechanisms such as transport. In this study, we find, besides the scale interactions, the transport process is crucial on the basic-flow window: KE is transported into the blocking region while APE is transported out of it.

REFERENCES

- Arai, M., and H. Mukougawa, 2002: On the effectiveness of the eddy straining mechanism for the maintenance of blocking flows. *J. Meteor. Soc. Japan*, **80**, 1089–1102, doi:10.2151/jmsj.80.1089.
- Austin, J. F., 1980: The blocking of middle latitude westerly winds by planetary waves. *Quart. J. Roy. Meteor. Soc.*, **106**, 327–350, doi:10.1002/qj.49710644807.
- Barriopedro, D., R. García-Herrera, A. R. Lupo, and E. Hernández, 2006: A climatology of Northern Hemisphere blocking. *J. Climate*, **19**, 1042–1063, doi:10.1175/JCLI3678.1.
- Berggren, R., B. Bolin, and C.-G. Rossby, 1949: An aerological study of zonal motion, its perturbations and break-down. *Tellus*, **1**, 14–37, doi:10.3402/tellusa.v1i2.8501.
- Branstator, G., 1987: A striking example of the atmosphere's leading traveling pattern. *J. Atmos. Sci.*, **44**, 2310–2323, doi:10.1175/1520-0469(1987)044<2310:ASEOTA>2.0.CO;2.
- Charney, J. G., and J. G. DeVore, 1979: Multiple flow equilibria in the atmosphere and blocking. *J. Atmos. Sci.*, **36**, 1205–1216, doi:10.1175/1520-0469(1979)036<1205:MFEITA>2.0.CO;2.
- Charney, J. S., J. Shukla, and K. C. Mo, 1981: Comparison of a barotropic blocking theory with observation. *J. Atmos. Sci.*, **38**, 762–779, doi:10.1175/1520-0469(1981)038<0762:COABBT>2.0.CO;2.
- Colucci, S. J., 1985: Explosive cyclogenesis and large-scale circulation changes: Implications for atmospheric blocking. *J. Atmos. Sci.*, **42**, 2701–2717, doi:10.1175/1520-0469(1985)042<2701:ECALSC>2.0.CO;2.
- Fournier, A., 2000: Introduction to orthonormal wavelet analysis with shift invariance: Application to observed atmospheric blocking spatial structure. *J. Atmos. Sci.*, **57**, 3856–3880, doi:10.1175/1520-0469(2000)057<3856:ITOWAW>2.0.CO;2.
- , 2002: Atmospheric energetics in the wavelet domain. Part I: Governing equations and interpretation for idealized flows. *J. Atmos. Sci.*, **59**, 1182–1197, doi:10.1175/1520-0469(2002)059<1182:AEITWD>2.0.CO;2.
- , 2003: Atmospheric energetics in the wavelet domain. Part II: Time-averaged observed atmospheric blocking. *J. Atmos. Sci.*, **60**, 319–338, doi:10.1175/1520-0469(2003)060<0319:AEITWD>2.0.CO;2.
- , 2005: Instantaneous wavelet energetic transfers between atmospheric blocking and local eddies. *J. Climate*, **18**, 2151–2171, doi:10.1175/JCLI3381.1.
- Green, J. S. A., 1977: The weather during July 1976: Some dynamical considerations of the drought. *Weather*, **32**, 120–126, doi:10.1002/j.1477-8696.1977.tb04532.x.
- Hansen, A. R., and T.-C. Chen, 1982: A spectral energetics analysis of atmospheric blocking. *Mon. Wea. Rev.*, **110**, 1146–1165, doi:10.1175/1520-0493(1982)110<1146:ASEAOA>2.0.CO;2.
- , and A. Sutera, 1984: A comparison of the spectral energy and enstrophy budgets of blocking versus nonblocking periods. *Tellus*, **36A**, 52–63, doi:10.1111/j.1600-0870.1984.tb00222.x.
- Holopainen, E., and C. Fortelius, 1987: High-frequency transient eddies and blocking. *J. Atmos. Sci.*, **44**, 1632–1645, doi:10.1175/1520-0469(1987)044<1632:HFTEAB>2.0.CO;2.
- Huang, F., X. Tang, S. Y. Lou, and C. Lu, 2007: Evolution of dipole-type blocking life cycles: Analytical diagnoses and observations. *J. Atmos. Sci.*, **64**, 52–73, doi:10.1175/JAS3819.1.
- Illari, L., 1984: A diagnostic study of the potential vorticity in a warm blocking anticyclone. *J. Atmos. Sci.*, **41**, 3518–3526, doi:10.1175/1520-0469(1984)041<3518:ADSOTP>2.0.CO;2.
- , and J. C. Marshall, 1983: On the interpretation of eddy fluxes during a blocking episode. *J. Atmos. Sci.*, **40**, 2232–2242, doi:10.1175/1520-0469(1983)040<2232:OTIOEF>2.0.CO;2.
- Jin, F.-F., L.-L. Pan, and M. Watanabe, 2006: Dynamics of synoptic eddy and low-frequency flow interaction. Part II: A theory for low-frequency modes. *J. Atmos. Sci.*, **63**, 1695–1708, doi:10.1175/JAS3716.1.
- Kushnir, Y., 1987: Retrograding wintertime low-frequency disturbances over the North Pacific Ocean. *J. Atmos. Sci.*, **44**, 2727–2742, doi:10.1175/1520-0469(1987)044<2727:RWLFDO>2.0.CO;2.
- Lejenäs, H., and H. Økland, 1983: Characteristics of Northern Hemisphere blocking as determined from a long time series of observational data. *Tellus*, **35A**, 350–362, doi:10.1111/j.1600-0870.1983.tb00210.x.
- Liang, X. S., 2016: Canonical transfer and multiscale energetics for primitive and quasi-geostrophic atmospheres. *J. Atmos. Sci.*, **73**, 4439–4468, doi:10.1175/JAS-D-16-0131.1.
- , and A. R. Robinson, 2005: Localized multiscale energy and vorticity analysis. *Dyn. Atmos. Oceans*, **38**, 195–230, doi:10.1016/j.dynatmoce.2004.12.004.
- , and D. Anderson, 2007: Multiscale window transform. *Multiscale Model. Simul.*, **6**, 437–467, doi:10.1137/06066895X.
- , and A. R. Robinson, 2007: Localized multi-scale energy and vorticity analysis: II. Finite-amplitude instability theory and validation. *Dyn. Atmos. Oceans*, **44**, 51–76, doi:10.1016/j.dynatmoce.2007.04.001.
- Lorenz, E. N., 1955: Available potential energy and the maintenance of the general circulation. *Tellus*, **7**, 157–167, doi:10.3402/tellusa.v7i2.8796.
- Lou, S. Y., and F. Huang, 2017: Alice-Bob physics: Coherent solutions of nonlocal KdV systems. *Sci. Rep.*, **7**, 869, doi:10.1038/s41598-017-00844-y.

- Luo, D., J. Cha, L. Zhong, and A. Dai, 2014: A nonlinear multiscale interaction model for atmospheric blocking: The eddy-blocking matching mechanism. *Quart. J. Roy. Meteor. Soc.*, **140**, 1785–1808, doi:10.1002/qj.2337.
- McWilliams, J. C., 1980: An application of equivalent modons to atmospheric blocking. *Dyn. Atmos. Oceans*, **5**, 43–66, doi:10.1016/0377-0265(80)90010-X.
- Michelangeli, P.-A., and R. Vautard, 1998: The dynamics of Euro-Atlantic blocking onsets. *Quart. J. Roy. Meteor. Soc.*, **124**, 1045–1070, doi:10.1002/qj.49712454803.
- Mullen, S. L., 1987: Transient eddy forcing of blocking flows. *J. Atmos. Sci.*, **44**, 3–22, doi:10.1175/1520-0469(1987)044<0003:TEFOBF>2.0.CO;2.
- Nakamura, H., M. Nakamura, and J. L. Anderson, 1997: The role of high- and low-frequency dynamics in blocking formation. *Mon. Wea. Rev.*, **125**, 2074–2093, doi:10.1175/1520-0493(1997)125<2074:TROHAL>2.0.CO;2.
- Namias, J., 1947: Extended forecasting by mean circulation methods. U.S. Weather Bureau Rep., 93 pp. [Available online at <http://hdl.handle.net/2027/uc1.31822031269715>.]
- Oort, A. H., 1964: On estimates of the atmospheric energy cycle. *Mon. Wea. Rev.*, **92**, 483–493, doi:10.1175/1520-0493(1964)092<0483:OEOTAE>2.3.CO;2.
- Park, T.-W., Y. Deng, W. Li, S. Yang, and M. Cai, 2015: Mass footprints of the North Pacific atmospheric blocking highs. *J. Climate*, **28**, 4941–4949, doi:10.1175/JCLI-D-14-00598.1.
- Pelly, J. L., and B. J. Hoskins, 2003: A new perspective on blocking. *J. Atmos. Sci.*, **60**, 743–755, doi:10.1175/1520-0469(2003)060<0743:ANPOB>2.0.CO;2.
- Rex, D. F., 1950a: Blocking action in the middle troposphere and its effect upon regional climate (I). An aerological study of blocking action. *Tellus*, **2**, 196–211.
- , 1950b: Blocking action in the middle troposphere and its effect upon regional climate (II). The climatology of blocking actions. *Tellus*, **2**, 275–301.
- Robinson, W. A., 1991: The dynamics of low-frequency variability in a simple model of the global atmosphere. *J. Atmos. Sci.*, **48**, 429–441, doi:10.1175/1520-0469(1991)048<0429:TDOLVF>2.0.CO;2.
- Sawyer, J. S., 1970: Observational characteristics of atmospheric fluctuations with a time scale of a month. *Quart. J. Roy. Meteor. Soc.*, **96**, 610–625, doi:10.1002/qj.49709641005.
- Schneidereit, A., S. Schubert, P. Vargin, F. Lunkeit, X. Zhu, D. H. W. Peters, and K. Fraedrich, 2012: Large-scale flow and the long-lasting blocking high over Russia: Summer 2010. *Mon. Wea. Rev.*, **140**, 2967–2981, doi:10.1175/MWR-D-11-00249.1.
- Shutts, G. J., 1983: The propagation of eddies in diffluent jetstreams: Eddy vorticity forcing of “blocking” flow fields. *Quart. J. Roy. Meteor. Soc.*, **109**, 737–761, doi:10.1002/qj.49710946204.
- Sousa, P. M., D. Barriopedro, R. M. Trigo, A. M. Ramos, R. Nieto, L. Gimeno, K. F. Turkman, and M. L. R. Liberato, 2016: Impact of Euro-Atlantic blocking patterns in Iberia precipitation using a novel high resolution dataset. *Climate Dyn.*, **46**, 2573–2591, doi:10.1007/s00382-015-2718-7.
- Tanaka, S., K. Nishii, and H. Nakamura, 2016: Vertical structure and energetics of the western Pacific teleconnection pattern. *J. Climate*, **29**, 6597–6616, doi:10.1175/JCLI-D-15-0549.1.
- Tibaldi, S., and F. Molteni, 1990: On the operational predictability of blocking. *Tellus*, **42A**, 343–365, doi:10.3402/tellusa.v42i3.11882.
- Treidl, R. A., E. C. Birch, and P. Sajecki, 1981: Blocking action in the Northern Hemisphere: A climatological study. *Atmos.–Ocean*, **19**, 1–23, doi:10.1080/07055900.1981.9649096.
- Trigo, R. M., I. F. Trigo, C. C. DaCamara, and T. J. Osborn, 2004: Climate impact of the European winter blocking episodes from the NCEP/NCAR Reanalyses. *Climate Dyn.*, **23**, 17–28, doi:10.1007/s00382-004-0410-4.
- Tsou, C.-H., and P. J. Smith, 1990: The role of synoptic/planetary-scale interactions during the development of a blocking anticyclone. *Tellus*, **42A**, 174–193, doi:10.3402/tellusa.v42i1.11869.
- Uppala, S. M., and Coauthors, 2005: The ERA-40 Re-Analysis. *Quart. J. Roy. Meteor. Soc.*, **131**, 2961–3012, doi:10.1256/qj.04.176.
- Woollings, T., B. Hoskins, M. Blackburn, and P. Berrisford, 2008: A new Rossby wave-breaking interpretation of the North Atlantic Oscillation. *J. Atmos. Sci.*, **65**, 609–626, doi:10.1175/2007JAS2347.1.
- Xu, F., and X. S. Liang, 2017: On the generation and maintenance of the 2012/13 sudden stratospheric warming. *J. Atmos. Sci.*, **74**, 3209–3228, doi:10.1175/JAS-D-17-0002.1.
- Yamazaki, A., and H. Itoh, 2013: Vortex–vortex interactions for the maintenance of blocking. Part I: The selective absorption mechanism and a case study. *J. Atmos. Sci.*, **70**, 725–742, doi:10.1175/JAS-D-11-0295.1.